Axisymmetric contour dynamics for buoyant vortex rings

Ching Chang [1]† and Stefan G. Llewellyn Smith[1,2]

[1]Department of Mechanical and Aerospace Engineering, Jacobs School of Engineering, UCSD, 9500 Gilman Drive, La Jolla, CA 92093-0411, USA

[2]Scripps Institution of Oceanography, UCSD, 9500 Gilman Drive, La Jolla, CA 92093-0213, USA

The present work uses a reduced order model to study the motion of a buoyant vortex ring with non-negligible core size. Buoyancy is considered in both non-Boussinesq and Boussinesq situations using an axisymmetric contour dynamics formulation. The density of the vortex ring differs from that of the ambient fluid, and both densities are constant and conserved. The motion of the ring is calculated by following the boundary of the vortex core, which is also the interface between the two densities. The velocity of the contour comes from a combination of a specific continuous vorticity distribution within its core and a vortex sheet on the core boundary. An evolution equation for the vortex sheet is derived from the Euler equation, which simplifies considerably in the Boussinesq limit. Numerical solutions for the coupled integro-differential equations are obtained. The dynamics of the vortex sheet and the formation of two possible singularities, including singularities in the curvature and the shock-like profile of the vortex sheet strength, are discussed. Three dimensionless groups, the Atwood, Froude and Weber numbers, are introduced to measure the importance of physical effects acting on the motion of a buoyant vortex ring.

1. Introduction

Vortex rings have attracted much attention from applied mathematicians and fluid dynamicists over the history of vortex dynamics. Early studies can be traced back to the work of Kelvin (1867) and Hicks (1884). Their theories for the steady motion of a vortex ring assumed that the core is small and circular. The vortex core refers to the region enclosed by a contour shown in figure 1. The area of that region allows us to define a vortex core radius a. If a is very small compared to the radius of the vortex ring about its axis of symmetry, we define it as a thin ring; otherwise the ring is "fat". A detailed description of the profile of the vortical core was missing until Fraenkel (1972) provided an asymptotic formulation for small cross-section rings. Norbury (1972) found steady "fat" vortex rings close to the Hill's spherical vortex. Norbury (1973) then connected the previous two solutions via a one-parameter family of steady vortex rings ranging from thin to fat rings. This solution has an azimuthal vorticity distribution inside the ring

† Email address for correspondence: chc054@eng.ucsd.edu

given by

$$\omega_\phi = r\Omega, \tag{1.1}$$

where r is the radial distance to the axis of symmetry and Ω is constant. Then ω_ϕ satisfies the vorticity equation in axisymmetric geometry,

$$\frac{\mathrm{D}}{\mathrm{D}t}\left(\frac{\omega_\phi}{r}\right) = 0, \tag{1.2}$$

where $\mathrm{D}/\mathrm{D}t$ is the material derivative. We are using cylindrical coordinates (r, ϕ, z).

In general, classic vortex dynamics deals with incompressible, inviscid Euler flows. The flows are dominated by vorticity and the fluid density is set constant throughout. Shariff, Leonard & Ferziger (1989) provides a comprehensive review of vortex rings, while Shariff & Leonard (1992) has a clear discussion of the formation, dynamics, interactions and the stability of vortex rings. In many circumstances, e.g. in geophysical and environmental settings, fluid flows are not only governed by vorticity but also by other physical effects. The additional physics we want to address here is buoyancy, the combined effect of density difference and gravity. Well-known example of buoyant vortices are the bubble rings created and manipulated by dolphins (see Marten *et al.* 1996), which might be important to understand animal behaviour. One can also observe bubble rings created by human divers in the ocean or a swimming pool. A smoke ring can be created from a fireball or a thermal plume, and smoke rings expelled from a volcano have also been observed (Velasco Fuentes 2014). From a fluid dynamics perspective, the first study of buoyant vortex rings was the theoretical work and laboratory observations of Turner (1957). The theoretical study of Pedley (1968) confirmed Turner's finding of the expansion of a buoyant vortex ring in inviscid flows and predicted finite lifetimes for bubble rings. Chang & Llewellyn Smith (2018) calculated the motion of thin buoyant vortex filaments including a buoyant ring with a small inclination. However, these results are for thin vortex rings whose core size is much smaller than their radius.

Buoyant vortex rings with large cores have been studied theoretically and numerically by Lundgren & Mansour (1991) and Chen *et al.* (1999). Their calculations start from a spherical bubble rising due to buoyancy. The bubble is penetrated by the surrounding fluid from its bottom because of the gradient of hydrostatic pressure and then changes its topology to a bubble ring. Lundgren & Mansour (1991) used a boundary-integral method based on potential theory to calculate the motion of bubbles before and after they turned into rings. A model equation similar to that in Turner (1957) and Pedley (1968) was used when the vortex ring became very thin at later times. Chen *et al.* (1999) used the incompressible Navier–Stokes equations to calculate the transition from a spherical bubble to a bubble ring numerically. Another numerical study by Cheng, Lou & Lim (2013) carried out three-dimensional DNS that showed that a bubble ring is eventually destroyed by instability. The recent experimental studies of Vasel-Be-Hagh, Carriveau & Ting (2015*a*) and Vasel-Be-Hagh *et al.* (2015*b*) investigate the formation and the dynamics of bubble rings along with the viscous drag acting on a buoyant vortex ring.

Here we use a contour dynamics method in axisymmetric geometry to study buoyant vortex rings. Contour dynamics was first used by Zabusky, Hughes & Roberts (1979) to calculate the nonlinear evolution of a vortex patch in two dimensions. It was later adapted to axisymmetry in Pozrikidis (1986); Shariff *et al.* (1989); see also Riley (1998) and Shariff, Leonard & Ferziger (2008). A detailed description and numerical techniques of the method can be found in Dritschel (1989) and in the review of Pullin (1992). Blyth *et al.* (2014) showed that buoyancy enters the vorticity equation through the

baroclinic term. To take account of buoyancy, we assign constant densities ρ_1, ρ_2 to the surrounding fluid and the vortex ring respectively. The density gradient becomes a Dirac delta function on the interface and the baroclinic torque is zero everywhere except on the interface. As a result, vorticity is generated on the interface and forms a vortex sheet. An evolution equation for the vortex sheet is essential for buoyancy to be included into the contour dynamics formulation. Other additional physics such as magnetic force (see Hattori & Moffatt 2006; Llewellyn Smith & Hattori 2012) also enters in the form of a vortex sheet. A review of contour dynamics method with additional physics can be found in Llewellyn Smith *et al.* (2018). The evolution equation for vortex sheet strength between different density fluids can be found in Baker *et al.* (1982) and Baker & Xie (2011) for two-dimensional free-surface waves. A similar formulation was used with gravity absent in Sohn & Hwang (2005) and Shin, Sohn & Hwang (2018) for two-density flows. Tryggvason (1988) and Stock, Dahm & Tryggvason (2008) derived an evolution equation for a vortex sheet to investigate the problems of Rayleigh–Taylor instability and the interaction between vortices and a density interface.

Surface tension can also be important in the dynamics of buoyant vortex rings, and the vortex sheet equation will contain a term representing surface tension. Studies including surface tension in the vortex sheet dynamics are Baker & Nachbin (1998), Shin, Sohn & Hwang (2014), Sohn (2015) and Shin *et al.* (2018). Most studies solve two-dimensional problems and with an initially straight line or a slightly perturbed vortex sheet, although Baker & Moore (1989) and Sohn (2015) study a circular vortex sheet in two dimensions.

In this paper, calculations for a vortex sheet in axisymmetry are carried out. In §2, we introduce axisymmetric contour dynamics and derive an evolution equation for the vortex sheet on the interface using the Euler equation. The relevant dimensionless numbers in this problem are also discussed. In §3, we present our numerical approaches for solving the coupled integro-differential equations in axisymmetric domain. Numerical results are presented in §4. We conclude in §5.

2. Mathematical formulation

We consider a buoyant vortex ring in an ideal fluid. The governing equations are

$$\boldsymbol{\nabla} \cdot \mathbf{u} = 0, \tag{2.1}$$

$$\rho \frac{\mathrm{D}\mathbf{u}}{\mathrm{D}t} = -\boldsymbol{\nabla}p + \rho\mathbf{g}. \tag{2.2}$$

The cross-section of a vortex ring core forms a confined region in the *r*-*z* plane (see figure 1) and the vorticity is zero everywhere except inside or on this contour. The contour is material and represented by a parameterized curve $\mathbf{R}$. Its evolution determines the motion of the axisymmetric vortex ring. The flow is axisymmetric without swirl, so the velocity field and the vorticity field are $\mathbf{u} = (u_r, 0, u_z)$ and $\boldsymbol{\omega} = (0, \omega_\phi, 0)$, respectively. We can calculate the motion by evolving the contour using

$$\frac{\mathrm{d}\mathbf{R}}{\mathrm{d}t} = \mathbf{u}, \tag{2.3}$$

where the velocity is

$$u_r = -\frac{1}{r}\frac{\partial \psi}{\partial z}, \qquad u_z = \frac{1}{r}\frac{\partial \psi}{\partial r}. \tag{2.4}$$

The Stokes streamfunction is given by

$$\psi(r, z, t) = \iint \omega_\phi(r', z', t) G(r, z | r', z') \,\mathrm{d}r' \,\mathrm{d}z', \tag{2.5}$$

and satisfies the equation

$$\frac{1}{r}\left(\frac{\partial^2}{\partial r^2}-\frac{1}{r}\frac{\partial}{\partial r}+\frac{\partial^2}{\partial z^2}\right)\psi=-\omega_\phi. \tag{2.6}$$

This differential equation is solved using the Green's function

$$G(r,z|r',z')=\frac{\sqrt{rr'}}{2\pi}\left[\left(\frac{2}{k}-k\right)K(k)-\frac{2}{k}E(k)\right], \tag{2.7}$$

where

$$k^2=\frac{4rr'}{(r+r')^2+(z-z')^2}. \tag{2.8}$$

Here $K(k)$ and $E(k)$ are the complete elliptic integrals of the first and second kind respectively. The double integral in (2.5) is transformed into a contour integral using Green's theorem and the velocity field in (2.4) is obtained. The velocity on the boundary is then evaluated and the contour is evolved in time. This technique is called contour dynamics. More details of contour dynamics calculation for vortex rings can be found in Pozrikidis (1986); Shariff *et al.* (1989); Riley (1998) and Shariff *et al.* (2008).

If a vortex sheet is present on the interface, the velocity will consist of contributions from both the vortex sheet on the interface and the continuous vorticity inside. The latter is referred to as a vortex patch. For a classic vortex ring with one density throughout the flow, there is only a vortex patch. Riley (1998) gives a good discussion of axisymmetric vortex patches. The continuous vorticity distribution is taken to be $\omega_\phi=r\Omega$, where Ω is a constant (see §1). Using Green's theorem gives the contour integrals

$$\mathbf{u}_p(r,z)=\frac{\Omega}{r}\oint G\cos\theta'r'\,\mathrm{d}s'\,\hat{\mathbf{r}}+\Omega\oint[H\cos\theta'(z'-z)-G\sin\theta']\,\mathrm{d}s'\,\hat{\mathbf{z}}, \tag{2.9}$$

where s is the arc length and $\theta(r,z)$ is the angle between the outward normal to the interface and the unit vector in z (see figure 1). All variables with primes in the integral are functions of (r',z'). The function G is given in (2.7), while

$$H(r,z|r',z')=\frac{r'K(k)}{\pi\sqrt{(r+r')^2+(z-z')^2}}. \tag{2.10}$$

For the vortex sheet, carrying out the integral in (2.5) along the interface and using (2.4) gives the self-induced velocity of a vortex sheet with strength γ as (see Hattori & Moffatt 2006)

$$\mathbf{u}_s(r,z)=-\frac{1}{r}\oint\frac{\partial G}{\partial z}\gamma'\,\mathrm{d}\xi'\,\hat{\mathbf{r}}+\frac{1}{r}\oint\frac{\partial G}{\partial r}\gamma'\,\mathrm{d}\xi'\,\hat{\mathbf{z}}, \tag{2.11}$$

where ξ is a parameterisation without any specific physical significance that increases clockwise along the contour (see figure 1). The contour is evolved using $\mathbf{u}=\mathbf{u}_p+\mathbf{u}_s$ in (2.3).

2.1. *The non-Boussinesq case*

For a vortex ring whose density differs from that of the environment, the density jump on the interface results in baroclinic generation of vorticity. Baroclinic torque creates a vortex sheet on the interface. In axisymmetric geometry, the vortex sheet is composed of vorticity perpendicular to the r-z plane, i.e. in the azimuthal direction. The interface can be written as a closed curve $\mathbf{R}=(R(\xi,t),Z(\xi,t))$, where ξ is the parameterisation
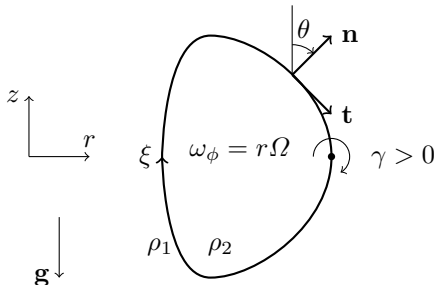
Figure 1: A schematic illustration of the contour in axisymmetric domain; ω_ϕ and γ are positive into the plane. The parameterisation ξ goes clockwise.

introduced earlier. The local tangent and normal vectors are

$$\mathbf{t} = \frac{\partial \mathbf{R}}{\partial \xi} \left| \frac{\partial \mathbf{R}}{\partial \xi} \right|^{-1}, \qquad \mathbf{n} = \frac{\partial \mathbf{t}}{\partial s} \kappa^{-1}, \tag{2.12}$$

where κ is the curvature, s is arclength, and

$$\frac{\partial s}{\partial \xi} = \left| \frac{\partial \mathbf{R}}{\partial \xi} \right| = L \tag{2.13}$$

is the arc length metric. The normal vector points out of the vortex.

On either side of the interface, the densities are ρ_1 and ρ_2, where the subscripts 1 and 2 indicate outside and inside. The corresponding velocities are $\mathbf{u}_1$, $\mathbf{u}_2$ and the vortex sheet strength is defined by $\gamma = L(\mathbf{u}_1 - \mathbf{u}_2) \cdot \mathbf{t}$. The tangential velocity on the interface is given by averaging velocities from either side, $\bar{\mathbf{u}} = (\mathbf{u}_1 + \mathbf{u}_2)/2$. A Lagrangian velocity following material points is defined by

$$\widetilde{\mathbf{u}} = \bar{\mathbf{u}} + \alpha \frac{\gamma}{2L} \mathbf{t}. \tag{2.14}$$

For $\alpha = 1$ or -1, the material points follow the motion of outside or inside fluid respectively (see Baker *et al.* 1982). Then velocities on either side of the interface are

$$\mathbf{u}_1 = \bar{\mathbf{u}} + \frac{\gamma}{2L} \mathbf{t} = \widetilde{\mathbf{u}} + (1 - \alpha) \frac{\gamma}{2L} \mathbf{t}, \qquad \mathbf{u}_2 = \bar{\mathbf{u}} - \frac{\gamma}{2L} \mathbf{t} = \widetilde{\mathbf{u}} - (1 + \alpha) \frac{\gamma}{2L} \mathbf{t}. \tag{2.15}$$

Evaluating the Euler equation on both sides gives

$$\frac{\partial \mathbf{u}_1}{\partial t} + (\mathbf{u}_1 \cdot \boldsymbol{\nabla}) \mathbf{u}_1 = -\frac{1}{\rho_1} \boldsymbol{\nabla} p + \mathbf{g}, \tag{2.16}$$

$$\frac{\partial \mathbf{u}_2}{\partial t} + (\mathbf{u}_2 \cdot \boldsymbol{\nabla}) \mathbf{u}_2 = -\frac{1}{\rho_2} \boldsymbol{\nabla} p + \mathbf{g}. \tag{2.17}$$

We follow the procedure in Baker *et al.* (1982) to eliminate pressure. We first subtract (2.17) from (2.16) and replace $\mathbf{u}_1$ and $\mathbf{u}_2$ in the advection term by $\widetilde{\mathbf{u}}$ from (2.15), giving

$$\frac{\mathrm{d}}{\mathrm{d}t} \left(\frac{\gamma}{L} \mathbf{t} \right) + \frac{\gamma}{L} \mathbf{t} \cdot \boldsymbol{\nabla} \widetilde{\mathbf{u}} - \alpha \frac{\gamma}{L} \mathbf{t} \cdot \boldsymbol{\nabla} \left(\frac{\gamma}{L} \mathbf{t} \right) = - \left(\frac{1}{\rho_1} - \frac{1}{\rho_2} \right) \boldsymbol{\nabla} p. \tag{2.18}$$

A material derivative following Lagrangian points is defined as

$$\frac{\mathrm{d}}{\mathrm{d}t} = \frac{\partial}{\partial t} + (\widetilde{\mathbf{u}} \cdot \boldsymbol{\nabla}). \tag{2.19}$$

Similarly, adding (2.16) and (2.17) together, and replacing $\mathbf{u}_1$ and $\mathbf{u}_2$ by $\widetilde{\mathbf{u}}$ and $\bar{\mathbf{u}}$ gives

$$2\frac{\mathrm{d}\bar{\mathbf{u}}}{\mathrm{d}t} - \alpha\frac{\gamma}{L}\mathbf{t}\cdot\boldsymbol{\nabla}\bar{\mathbf{u}} + \frac{\gamma}{2L}\mathbf{t}\cdot\boldsymbol{\nabla}\left(\frac{\gamma}{L}\mathbf{t}\right) = -\left(\frac{1}{\rho_2} + \frac{1}{\rho_1}\right)\boldsymbol{\nabla}p + 2\mathbf{g}. \tag{2.20}$$

The ratio between the coefficients of the pressure gradient in (2.18) and (2.20) is the Atwood number

$$A = \frac{\rho_1 - \rho_2}{\rho_1 + \rho_2}. \tag{2.21}$$

Eliminating the pressure yields

$$\frac{\mathrm{d}}{\mathrm{d}t}\left(\frac{\gamma}{L}\mathbf{t}\right) + \frac{\gamma}{L}\mathbf{t}\cdot\boldsymbol{\nabla}\widetilde{\mathbf{u}} - \alpha\frac{\gamma}{L}\mathbf{t}\cdot\boldsymbol{\nabla}\left(\frac{\gamma}{L}\mathbf{t}\right) = -2A\left[\frac{\mathrm{d}\bar{\mathbf{u}}}{\mathrm{d}t} - \frac{\alpha}{2}\frac{\gamma}{L}\mathbf{t}\cdot\boldsymbol{\nabla}\bar{\mathbf{u}} + \frac{\gamma}{4L}\mathbf{t}\cdot\boldsymbol{\nabla}\left(\frac{\gamma}{L}\mathbf{t}\right) - \mathbf{g}\right]. \tag{2.22}$$

To simplify the equation above, it can be shown that

$$\frac{1}{L}\frac{\mathrm{d}L}{\mathrm{d}t} = \mathbf{t}\cdot[(\mathbf{t}\cdot\boldsymbol{\nabla})\widetilde{\mathbf{u}}], \qquad \mathbf{t}\cdot\boldsymbol{\nabla} = \frac{1}{L}\frac{\partial}{\partial\xi}. \tag{2.23}$$

By projecting (2.22) on the tangential direction and using the Frenet–Serret formulas,

$$\frac{1}{L}\frac{\partial\mathbf{t}}{\partial\xi} = \kappa\mathbf{n}, \quad \frac{1}{L}\frac{\partial\mathbf{n}}{\partial\xi} = -\kappa\mathbf{t}, \tag{2.24}$$

we obtain

$$\frac{\mathrm{d}\gamma}{\mathrm{d}t} - \frac{\alpha}{2}\frac{\partial}{\partial\xi}\left(\frac{\gamma}{L}\right)^2 = -2AL\left[\mathbf{t}\cdot\frac{\mathrm{d}\bar{\mathbf{u}}}{\mathrm{d}t} - \frac{\alpha}{2}\frac{\gamma}{L^2}\frac{\partial\bar{\mathbf{u}}}{\partial\xi}\cdot\mathbf{t} + \frac{1}{8}\frac{1}{L}\frac{\partial}{\partial\xi}\left(\frac{\gamma}{L}\right)^2 - \mathbf{t}\cdot\mathbf{g}\right]. \tag{2.25}$$

This equation agrees with equation (2.15) in Baker *et al.* (1982), although their problem is two-dimensional and they use complex variables and Bernoulli's equation. We can match each term to their two-dimensional formulation, so the vortex sheet dynamics are the same in two-dimensional and axisymmetric flows. In this paper, we set $\alpha = 0$, i.e. we follow material points on the mean velocity so that $\widetilde{\mathbf{u}} = \bar{\mathbf{u}}$. We now drop the tildes and bars to obtain

$$\frac{\mathrm{d}\gamma}{\mathrm{d}t} = -2AL\left[\mathbf{t}\cdot\frac{\mathrm{d}\mathbf{u}}{\mathrm{d}t} + \frac{1}{8}\frac{1}{L}\frac{\partial}{\partial\xi}\left(\frac{\gamma}{L}\right)^2 - \mathbf{t}\cdot\mathbf{g}\right]. \tag{2.26}$$

A similar equation can also be found in Shin *et al.* (2018), although gravity is omitted in their formulation.

The evolution equation for γ is coupled with (2.9) and (2.11). These equations can be transformed into a Fredholm integral equation of the second kind for $\mathrm{d}\gamma/\mathrm{d}t$. Using (2.9), (2.11) and the definition of the unit tangent, we have

$$\begin{aligned}
\mathbf{t}\cdot\frac{\mathrm{d}\mathbf{u}}{\mathrm{d}t} &= \mathbf{t}\cdot\frac{\mathrm{d}\mathbf{u}_p}{\mathrm{d}t} + \mathbf{t}\cdot\frac{\mathrm{d}\mathbf{u}_s}{\mathrm{d}t} \\
&= \frac{1}{R}\left(-\frac{1}{L}\frac{\partial R}{\partial\xi}\oint\frac{\mathrm{d}\gamma'}{\mathrm{d}t}\frac{\partial G}{\partial Z}\mathrm{d}\xi' + \frac{1}{L}\frac{\partial Z}{\partial\xi}\oint\frac{\mathrm{d}\gamma'}{\mathrm{d}t}\frac{\partial G}{\partial R}\mathrm{d}\xi'\right) + f(R, Z, \gamma, \mathbf{u}),
\end{aligned} \tag{2.27}$$

where f is a function of R, Z, γ and $\mathbf{u}$, provided in Appendix A. The evolution equation of $\mathrm{d}\gamma/\mathrm{d}t$ is coupled with the Lagrangian advection equation in (2.3).

2.2. *The Boussinesq limit*

When the density difference across the interface is small but gravity remains important, we may assume $\rho_1 \approx \rho_2$ in all terms except for gravity. This is the Boussinesq

approximation. The evolution equation for γ in the Boussinesq limit is

$$\frac{d\gamma}{dt} = 2AL\mathbf{t} \cdot \mathbf{g} = \left(1 - \frac{\rho_2}{\bar{\rho}}\right) L\mathbf{t} \cdot \mathbf{g}, \tag{2.28}$$

where $\bar{\rho} = (\rho_1 + \rho_2)/2$ (other definitions are possible). In the Boussinesq approximation, the acceleration term $\mathbf{t} \cdot (d\mathbf{u}/dt)$ vanishes in the vortex sheet equation. This gives an advantage in solving the integro-differential equations numerically, since $d\gamma/dt$ is no longer determined by a Fredholm integral function and can be integrated by straightforward time-stepping.

2.3. *Surface tension*

When a vortex ring consists of air or vapor inside a liquid, the pressure is discontinuous across the interface. This dynamical jump is balanced by surface tension T_s,

$$p_2 - p_1 = \kappa T_s, \tag{2.29}$$

where κ is the curvature of the interface. Typically T_s is a constant. We can replace the pressure in (2.16) and (2.17) by p_1 and $p_1 + \kappa T_s$, respectively, then carry out the same calculation as in § 2.1. We obtain

$$\frac{d\gamma}{dt} = -2AL\left[\mathbf{t} \cdot \frac{d\mathbf{u}}{dt} + \frac{1}{8}\frac{1}{L}\frac{\partial}{\partial \xi}\left(\frac{\gamma}{L}\right)^2 - \mathbf{t} \cdot \mathbf{g}\right] + \frac{T_s}{\bar{\rho}}\frac{\partial \kappa}{\partial \xi}. \tag{2.30}$$

The rate of change of the vortex sheet strength contains a contribution proportional to the gradient of curvature along the interface when surface tension is present.

2.4. *Dimensionless parameters*

There are four dimensionless parameters for this problem. One is the aspect ratio of the ring, $S = a_0/\mathcal{R}_0$, where a_0 is the initial radius of vorticity core and $\mathcal{R}_0$ is the initial radius of vortex ring. Another dimensionless number can be taken as the Froude number

$$Fr = \frac{U_c}{\sqrt{ga_0}}, \tag{2.31}$$

where U_c is a velocity scale. We set $U_c = a_0^2\Omega$, which characterizes the translation of a homogeneous ring. The time scale is $a_0/U_c = 1/(a_0\Omega)$. The vortex sheet strength γ can be scaled by a_0U_c while ξ has no dimension. A dimensionless form of (2.30) is then given by

$$\frac{d\gamma}{dt} = -2AL\left[\mathbf{t} \cdot \frac{d\mathbf{u}}{dt} + \frac{1}{8}\frac{1}{L}\frac{\partial}{\partial \xi}\left(\frac{\gamma}{L}\right)^2 + \frac{1}{Fr^2}\mathbf{t} \cdot \hat{\mathbf{z}}\right] + \frac{1}{We}\frac{\partial \kappa}{\partial \xi}, \tag{2.32}$$

where gravity $\mathbf{g} = -g\hat{\mathbf{z}}$. The last parameter in the dimensionless equation is the Weber number,

$$We = \frac{\bar{\rho}U_c^2 a_0}{T_s} \tag{2.33}$$

A special case is $\Omega = 0$, when there is no continuous vorticity inside the vortex. We then choose the velocity scale using $U_c = \sqrt{ga_0}$, giving $Fr = 1$.

We call the third term on the right-hand side of (2.32) the buoyancy or source term, since vorticity is created by baroclinic generation. The second term on the right-hand side is the quadratic or nonlinear term. The first term is the dynamic-coupling term, in which the dynamics of the contour is coupled to the evolution of the sheet strength. The last term corresponds to surface tension.

	Domain	Density difference	Body force	Surface tension	Vortex patch
Baker *et al.* (1982)	2D	yes	gravity	no	no
Krasny (1986*a*)	2D	no	no	no	no
Baker *et al.* (1993)	2D	yes	gravity	no	no
Hou, Lowengrub & Shelley (1994)	2D	yes	gravity	yes	no
Baker & Nachbin (1998)	2D	no	no	yes	no
Baker & Xie (2011)	2D	yes	gravity	no	no
Shin *et al.* (2018)	2D	yes	no	yes	no
Pozrikidis (1986)	axisymm	no	no	no	yes
Shariff *et al.* (1989)	axisymm	no	no	no	yes
Nitsche & Krasny (1994)	axisymm	no	no	no	no
Nitsche (2001)	axisymm	no	no	no	no
Hattori & Moffatt (2006)	axisymm	no	magnetic	no	no
Llewellyn Smith & Hattori (2012)	axisymm	no	magnetic	no	yes
Present work	axisymm	yes	gravity	no	yes

Table 1: Previous studies on vortex sheet evolution compared to present work.

3. Numerical method

Before we start our discussion of the numerical scheme, it is worth surveying the literature to identify similar problems that have been investigated. In table 1 we list some references with calculations of vortex sheet evolution. The vortex sheet strength does not evolve when density differences, body forces and surface tension all vanish. Once density differences are introduced, the dynamic-coupled and quadratic terms in (2.32) are nonzero. Body forces behave like a source in (2.32). The self-induced velocity of the vortex sheet is calculated using the Biot–Savart law. If a vortex sheet is a closed contour enclosing vorticity, the contribution from vortex patch (2.9) must be added.

Our numerical scheme consists of four main parts: an interpolation method to approximate the location of the contour and compute spatial derivatives, quadrature to evaluate contour integrals, an integral equation to obtain the vortex sheet strength and a time-stepping method to evolve the contour. The contour is discretised using a set of Lagrangian points, i.e. material points, $\mathbf{X}_n$ in the r-z plane with $n = 1, 2, \ldots, N$. The initial contour is given by

$$R(\xi, 0) = \mathcal{R}_0 + a_0 \cos \xi, \ Z(\xi, 0) = a_0 \sin \xi \qquad (3.1)$$

for $\xi \in [0, 2\pi)$; $\mathcal{R}_0$ is the initial radius of the ring and a_0 is the radius of its core. For small ring sizes, this is almost the steadily propagating solution of Norbury (1973). We set $\mathcal{R}_0 = 1$ in all calculations. These Lagrangian points are evolved using (2.3),

$$\frac{\mathrm{d}\mathbf{X}_n}{\mathrm{d}t} = \mathbf{u}_n, \qquad (3.2)$$

where $\mathbf{u}_n$ is $\mathbf{u}$ evaluated numerically on $\mathbf{X}_n$.

3.1. *Interpolation and spatial differentiation*

Since the contour is a closed curve, it is natural to use a Fourier series to interpolate between points,

$$\mathbf{R}(\xi) = \sum_{k=-N/2}^{N/2-1} \hat{\mathbf{X}}_k \, \mathrm{e}^{\mathrm{i}k\xi}, \qquad (3.3)$$

where the $\hat{\mathbf{X}}_k$ are the Fourier coefficients of the Lagrangian points' locations. Here $k = -N/2,\ldots, -1, 0, 1,\ldots, N/2-1$ are the wavenumbers. The parameter ξ is equally spaced in $[0, 2\pi)$. The mth derivative along the contour is computed from the Fourier series

$$\mathbf{R}^{(m)}(\xi) = \sum_{k=-N/2}^{N/2-1} (\mathrm{i}k)^m \hat{\mathbf{X}}_k \, \mathrm{e}^{\mathrm{i}k\xi}. \qquad (3.4)$$

The spatial distribution of the vortex sheet strength γ_n is also interpolated using Fourier series. A Fourier filter is used to cut off the highest one-third of the spectrum to mitigate the the aliasing error from the quadratic term.

$$\hat{f}(k) = \begin{cases} 1, & |k| \leqslant N/3 \\ 0, & |k| > N/3, \end{cases} \qquad (3.5)$$

The aliasing error from the quadratic term can also be mitigated. A filter proposed by Krasny (1986*b*) is also implemented to suppress the growth of noise due to round-off error using a threshold of $O(10^{-12})$. At every time step, filters are applied whenever the time derivatives, $\mathbf{u}$ and $\mathrm{d}\gamma/\mathrm{d}t$, are obtained. Krasny's filter is applied first, then (3.5) right after it. Once the time derivatives are filtered, (R, Z) and γ are marched forward by one time step and the same filtering process applied to the new (R, Z) and γ.

3.2. *Quadrature rule*

The velocity $\mathbf{u}$ for each material point is the sum of (2.9) and (2.11), in which the contour integrals are computed numerically. The quadrature can be done using the trapezoidal rule which gives spectral convergence for periodic functions (Trefethen & Weideman 2014). However the functions G and H are singular as $(r', z') \to (r, z)$, because the complete elliptic integral of the first kind, $K(k)$, is unbounded when $k \to 1$. There are several ways to remove the singularity. One way is the vortex blob method (see Krasny 1986*a*): a small parameter ϵ is introduced into the denominator in (2.8), giving

$$k^2 = \frac{4rr'}{(r + r')^2 + (z - z')^2 + \epsilon^2}. \qquad (3.6)$$

The idea is essentially the same as the Moore–Rosenhead method (see Saffman 1992, p. 213) to desingularise the Biot–Savart integral for vortex filaments, in which a small parameter ϵ is added into denominator to avoid a division by zero. It acts to remove scales smaller than ϵ. The appropriate value of ϵ is discussed below.

A formally exact method is to subtract the singular part of the integrand. The regularised integral is then computed numerically using the trapezoidal rule. The asymptotic behavior of the singularity of (2.7) is (Pozrikidis 1986)

$$G_s \sim \frac{r'}{2\pi} \ln \frac{4}{\sqrt{1 - k^2}}. \qquad (3.7)$$

Shariff *et al.* (1989); Nitsche & Krasny (1994); Nitsche (2001); Hattori & Moffatt (2006); Llewellyn Smith & Hattori (2012) use this method to remove the singularity. A local
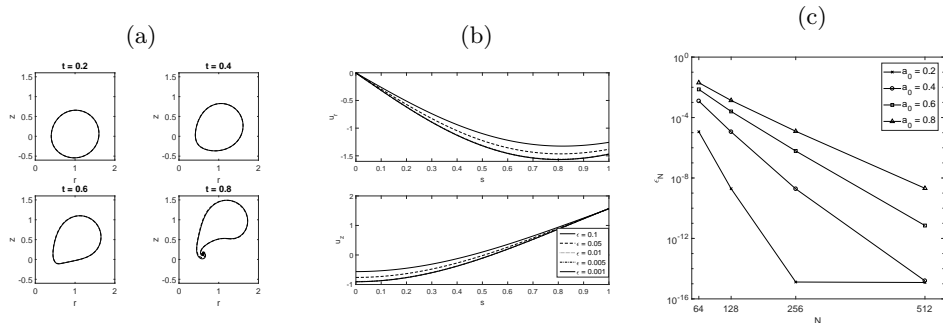
Figure 2: (a) Comparison of the blob method (solid line) and the series expansion method (dashed line) using velocity $\mathbf{u}_s$ only. $\epsilon = 0.01$; (b) a close look of velocity profile for various ϵ; (c) convergence test with different core size a_0.

series is then integrated term by term over segments adjacent to the singular point. Another method used in two dimensions (Baker *et al.* 1993; Hou *et al.* 1994; Baker & Xie 2011; Shin *et al.* 2018) is the trapezoidal rule based on alternative/mid points to avoid the singular point. This idea is not pursued here (but see §5).

While the series expansion method should formally yield higher accuracy, it suffers from two problems. First, the function takes a different form on the segment including the singularity which may reduce the accuracy of the trapezoidal rule. Second, it is difficult to implement when solving the dynamic-coupled term in the vortex sheet equation, since it requires a local approximation to $d\gamma/dt$, which is unknown. As a result, the blob method appears to be the most natural regularisation and is the one that was used. Nevertheless we can examine the difference between the two. The contours in figure 2(a) show very little difference using $\epsilon = 0.01$. Some differences can be noticed near the roll-up at $t = 0.8$, but the bulk motions of the two are almost the same. That serves our purpose well enough to model the motion of a buoyant vortex ring, even though the small scales are not perfectly resolved. We also test different value of ϵ. In figure 2(b), the profiles almost overlap for $\epsilon \leqslant 0.01$, and the maximum error of velocity profile is $O(10^{-6})$. The volume is a conserved quantity and the change in volume is 0.2% during $t = 0$–0.84 with $\epsilon = 0.01$. With $\epsilon = 0.05$ the computation lasts for a longer time $t = 0$–1.09 and the change in volume is 0.6%. In the present study, we used $\epsilon = 0.05$ in order to achieve longer integration in time.

The convergence test for $\mathbf{u}$ with respect to N uses the following approach: first we calculate the velocity $\mathbf{u}^{(N/2)}$ with grid resolution $N/2$, then we double the resolution to N by adding one new point between every two existing points. The velocity is then calculated again as $\mathbf{u}^{(N)}$. We compute the change in velocity at the original points, then take its norm as

$$\epsilon_N = ||\mathbf{u}^{(N)} - \mathbf{u}^{(N/2)}||. \tag{3.8}$$

We find $\epsilon_N \to 0$ when $N \to \infty$, where ϵ_N is a function of N and a_0 plotted in figure 2(c). Different initial vortex core radii a_0 require different values of N. If we set $\epsilon_N = 10^{-4}$ as our desired accuracy, $a_0 = 0.2$ satisfies this criterion with $N = 64$, while $a_0 = 0.8$ the required resolution rises to $N = 256$. Therefore, we choose $N = 64$ for $a_0 = 0.2$ and $N = 256$ for $a_0 = 0.8$, $N = 128$ for $a_0 = 0.4$ and $N = 256$ for $a_0 = 0.6$ to keep ϵ_N below 10^{-4}. For higher accuracy, e.g. $\epsilon_N < 10^{-8}$, $a_0 = 0.2$ needs resolution $N = 128$ and $a_0 = 0.8$ needs at least $N = 512$.

3.3. *Integral equation*

To solve for γ, the rate of change of γ is calculated by solving the integral equation given by combining (2.27) and (2.30):

$$\frac{\mathrm{d}\gamma}{\mathrm{d}t} = -2A\mathcal{L}\frac{\mathrm{d}\gamma}{\mathrm{d}t} + \mathcal{F}, \tag{3.9}$$

where the linear integral operator is

$$\mathcal{L}\frac{\mathrm{d}\gamma}{\mathrm{d}t} = \frac{1}{R}\left(-\frac{\partial R}{\partial \xi}\oint \frac{\partial G}{\partial Z}\frac{\mathrm{d}\gamma}{\mathrm{d}t}\,\mathrm{d}\xi' + \frac{\partial Z}{\partial \xi}\oint \frac{\partial G}{\partial R}\frac{\mathrm{d}\gamma}{\mathrm{d}t}\,\mathrm{d}\xi'\right)$$

and $\mathcal{F}$ contains all the terms on the right-hand side of (2.30) except the terms in $\mathrm{d}\gamma/\mathrm{d}t$. The Green function G is regularised by the blob method. The integral operator $\mathcal{L}$ is discretised using the trapezoidal rule and $\mathcal{F}_i$ is $\mathcal{F}$ evaluated at $\mathbf{X}_n$. Then (3.9) becomes

$$\left.\frac{\mathrm{d}\gamma}{\mathrm{d}t}\right|_i = -2A\sum_j \mathcal{L}_{ij}\left.\frac{\mathrm{d}\gamma}{\mathrm{d}t}\right|_j + \mathcal{F}_i. \tag{3.10}$$

The discretised equation can be transformed into the linear system

$$\left(\delta_{ij} + 2A\mathcal{L}_{ij}\right)\left.\frac{\mathrm{d}\gamma}{\mathrm{d}t}\right|_i = \mathcal{F}_i. \tag{3.11}$$

The matrix is diagonally dominant and (3.11) can be solved by successive over-relaxation (SOR) efficiently.

3.4. *Time-stepping*

Finally, $\mathbf{X}$ and γ are advanced in time using the classic four-stage Runge–Kutta scheme

$$\frac{\mathrm{d}\mathbf{X}}{\mathrm{d}t} = \frac{1}{6}\left[\mathbf{u}_{(1)} + 2\mathbf{u}_{(2)} + 2\mathbf{u}_{(3)} + \mathbf{u}_{(4)}\right], \tag{3.12}$$

where the $\mathbf{u}_{(j)}$ are intermediate values (e.g. see Iserles 2009, §3.2). The time step Δt is fixed at 0.001 in our calculations. The initial value of γ is zero. The two filters introduced earlier are also applied to intermediate values.

4. Numerical results

We first discuss the γ-equation and its solutions. We show the possible emergence of curvature singularities that limit the length of numerical calculations. Then we present numerical results and discuss their dependence on the dimensionless numbers A and Fr. Finally we quantify the motion of the ring using integral quantities.

4.1. *Boussinesq vs non-Boussinesq cases*

The evolution equation for γ, (2.32), is central when using axisymmetric contour dynamics to calculate the motion of buoyant vortex rings. The first two terms on the right-hand side of (2.32) are multiplied by the Atwood number A and represent the contribution from density difference alone. The third term with gravity has a prefactor A/Fr^2 which measures the strength of buoyancy. We exclude surface tension for now, so that $We \to \infty$. When the density difference is small but gravity is strong, we have $A \to 0$ but $A/Fr \gtrsim 1$. The problem can then be approximated by the Boussinesq formulation. For small Atwood number, e.g. $A = 0.01$, the vortex sheets evolved using (2.26) and (2.28) are almost identical (figure 3a). Profiles computed from both γ equations are very
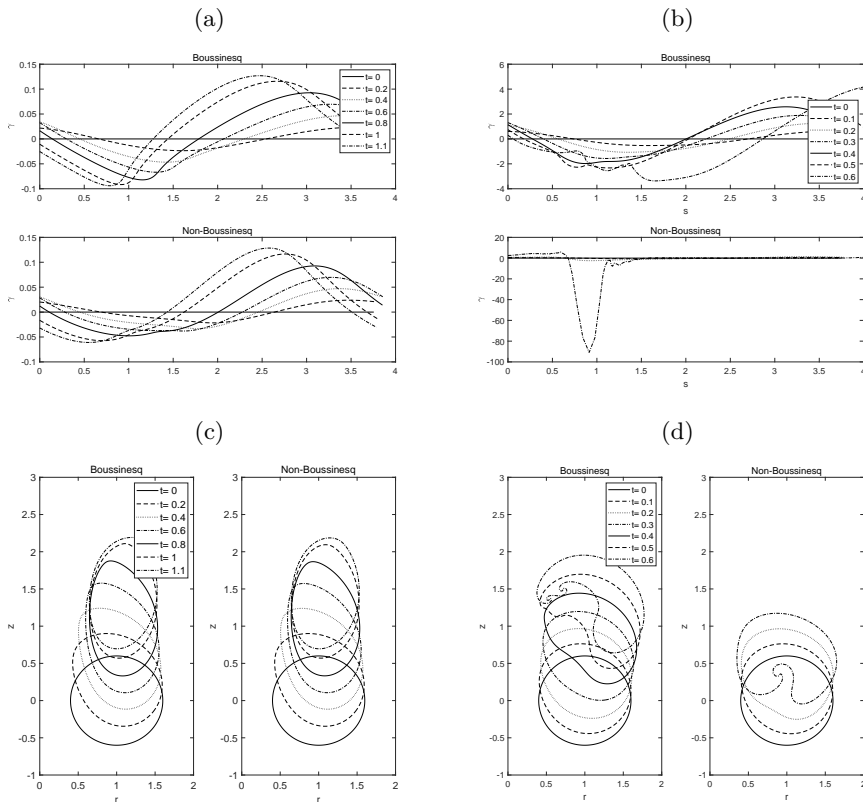
(a)   (b)

(c)   (d)

Figure 3: (a, b) The vortex sheet strength γ along the boundary and (c, d) the snapshots of contours. The Atwood numbers are $A = 0.01$, 0.5 for (a, c) and (b, d), respectively. All cases have $Fr = 1$ and $We = \infty$. For the Boussinesq case, γ is obtained using (2.28), while (2.26) is used for non-Boussinesq calculations.

similar, as shown in figure 3(c). Since A is small, the first two terms in the non-Boussinesq formulation are negligible.

We increase the Atwood number to 0.5. The solutions for γ are show in figure 3(b) and the corresponding contours in figure 3(d). The Boussinesq and non-Boussinesq cases differ when A is sufficiently large. The contour in the Boussinesq case have evolved into two roll ups when $t = 0.6$. The non-Boussinesq case is similar to the Boussinesq calculation before $t = 0.2$, but then the contour starts to deform more drastically than the Boussinesq case when $t > 0.2$. The non-Boussinesq calculation stops around $t = 0.3$ when the contour develops a sharp tip near $(0.92, 0.36)$ in figure 3(d) at which point the Fourier spectrum has saturated (see below), but before any roll-ups appear. The roll-ups are associated with the formation of finite-time singularity in curvature which has been found in many other studies on vortex sheet calculations.

4.2. *Singularities and vortex sheet dynamics for moderate A*

We plot the curvature of vortex sheets in the non-Boussinesq case for $A = 0.3$, 0.5 in figure 4. The formation of a spike in each case is apparent. This could indicate a finite-time curvature singularity as seen in the literature. The formation of curvature singularities of a vortex sheet was studied by Moore (1979). These singularities can be
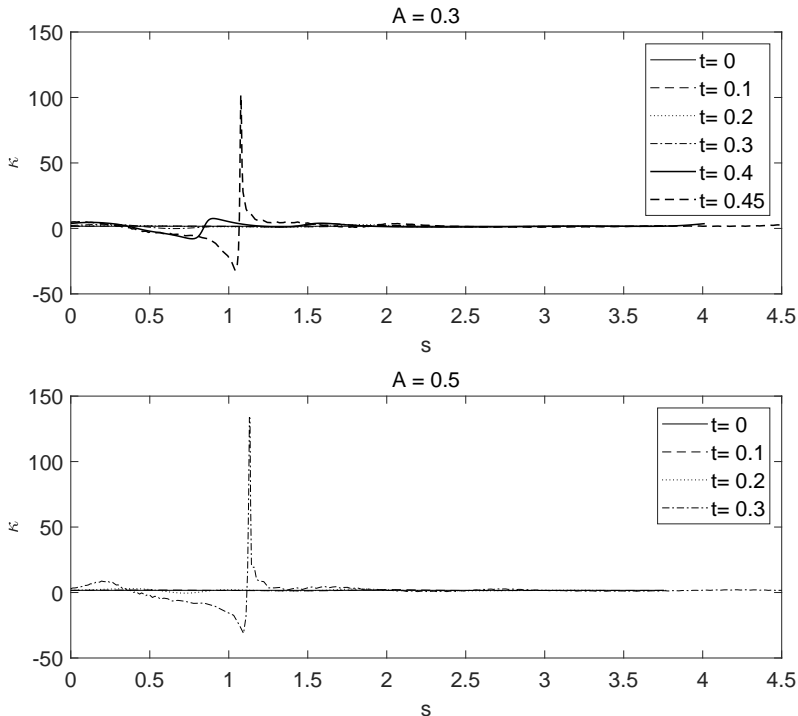
Figure 4: Curvature along the contour for $A = 0.3$ and 0.5. The height of the spike increases as A increases.

observed physically when singularities in the complex plane reach the real axis. Meiron, Baker & Orszag (1982) and Krasny (1986b) numerically confirmed Moore's asymptotic result. Cowley, Baker & Tanveer (1999) showed how singularities move in the complex plane and reach the real axis in finite time. Krasny (1986b) studied the formation of these singularities using the point–vortex approach, while Krasny (1986b) and Cowley *et al.* (1999) identified the singularity as having a $\frac{3}{2}$-power form. Baker *et al.* (1993) applied a vortex sheet model to the Rayleigh–Taylor instability problem, and showed that singularities do not reach the real axis in finite time if one layer of fluid has zero density (i.e. $A = 1$). These investigations considered two-dimensional periodic problems. The present calculation is axisymmetric, but the same kind of curvature singularity is possible. The nature of these singularities is worthy of a more detailed study, but that lies beyond the scope of this work as our intention is to calculate the motion of buoyant vortex rings. The reason we discuss singularities here is to point out that such a spike will cause a numerical blowup in our calculations. Even though our blob method may not allow actual singularity formation, the resulting growth in curvature appears strong enough to terminate the simulation for the values of ϵ required to obtain good overall numerical accuracy.

The Fourier spectrum of $\mathrm{d}\gamma/\mathrm{d}t$ in figure 5 shows the growth of higher modes. The spectrum still fills up when a filter is applied. The calculation blows up when the highest filtered mode, $|k| = N/3$, reaches the order of magnitude of the $|k| = 1$ mode. For the Boussinesq case, the highest mode grows but never exceeds the magnitude of mode $|k| = 1$ during the calculation. The difference between the vortex sheet evolution equations for the
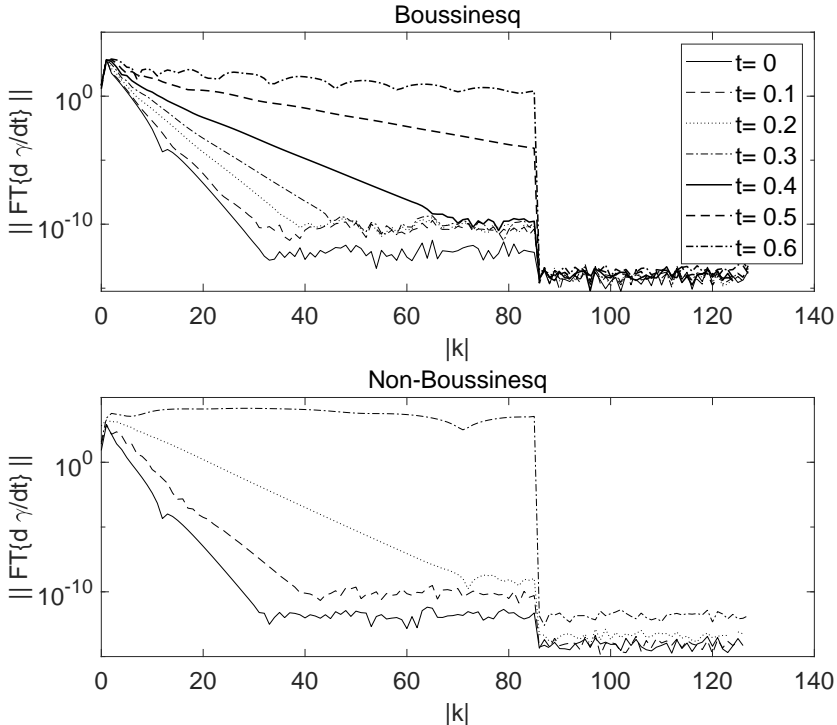
Figure 5: Fourier spectra of $\mathrm{d}\gamma/\mathrm{d}t$ for Boussinesq and non-Boussinesq calculations for $A = 0.5$, $Fr = 1$ and $We = \infty$, shown in figure 3(b) and (d). The calculations were stopped when the Fourier coefficient of highest mode becomes $\simeq O(1)$.

Boussinesq and non-Boussinesq cases comes from the first two terms in (2.26), which we now examine in detail. The behaviour of $\mathrm{d}\gamma/\mathrm{d}t$ is investigated by examining the evolution of each term in (2.26), as shown in figure 6. At $t = 0.1$, $\mathrm{d}\gamma/\mathrm{d}t$ is dominated by the source term (III), i.e. buoyancy, along with the dynamic-coupled term (I). The quadratic term (II) is small compared to the first two and negligible. As the calculation proceeds to $t = 0.2$, the dynamic-coupled term dominates $\mathrm{d}\gamma/\mathrm{d}t$ while the source terms become less important. The quadratic term became of the same order as the source term, and this is when the dynamics becomes more complicated. The contour in figure 3(d) starts to deviate from its initially circular shape. The sharp drop of vortex sheet strength profile near $s = 0.83$ indicates that a roll-up is beginning. In the plots at later times $t = 0.25$ and 0.3, the ratio of the source term diminished. At this moment, the entire dynamics is dominated by the sharp spike in the γ-profile, which is a combined contribution from the dynamic-couple and the quadratic terms. Note that while this is happening, the matrix on the left-hand side of the linear system (3.11) remains diagonally dominated, so that the linear system is well-conditioned.

4.3. *Non-Boussinesq vortex rings*

We first fix the aspect ratio at $S = 0.6$ for the following calculation. Our aim is to investigate how buoyancy alters the motion of the rings. Buoyancy is a result of combining density difference and gravity, and can be measured by A/Fr^2. We examine the terms on the right-hand side of (2.32). If A is small and Fr is large, buoyancy is negligible
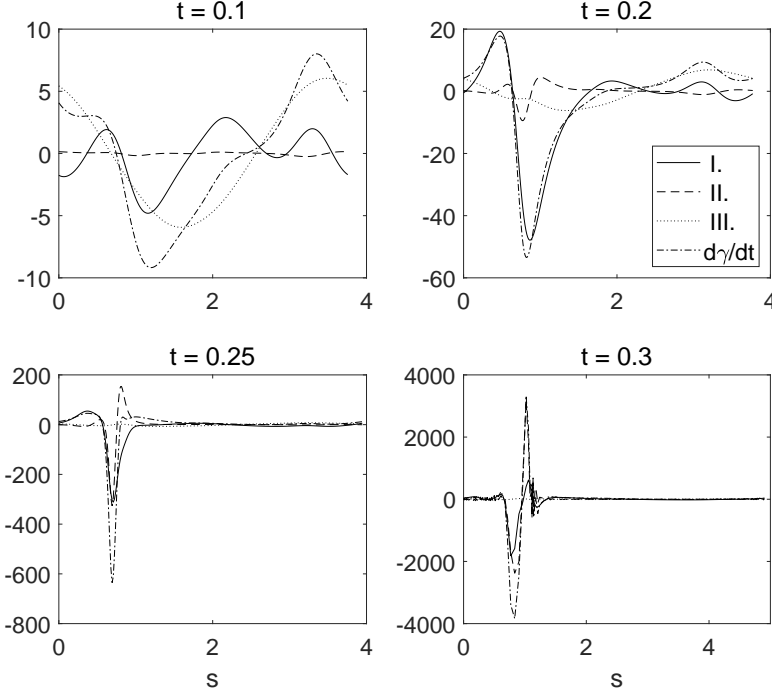
Figure 6: Terms in (2.26). Right-hand side terms are I: dynamic-coupled term, i.e. f in (2.27); II: quadratic term; III: buoyancy. $A = 0.5$ and $Fr = 1$. Their sum is $d\gamma/dt$.
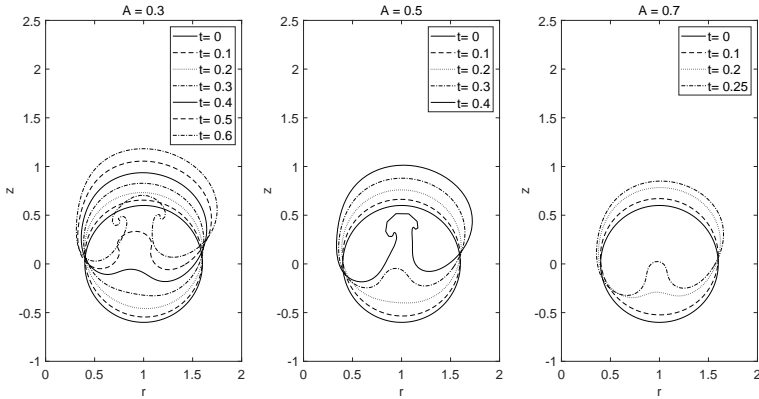

Figure 7: Evolution of contour with different Atwood numbers $A = 0.3$, 0.5, 0.7, from left to right respectively. Other parameters are kept constant: $S = 0.6$, $Fr = 0.3$ and $We = \infty$.

and $d\gamma/dt \approx 0$, so the vortex ring retains its classic solution. If Fr decreases such that A/Fr^2 equals or greater than $O(1)$, the buoyant vortex ring is in the Boussinesq limit. If A increases significantly, every term in the γ-equation become important and the vortex ring evolves in the non-Boussinesq regime.

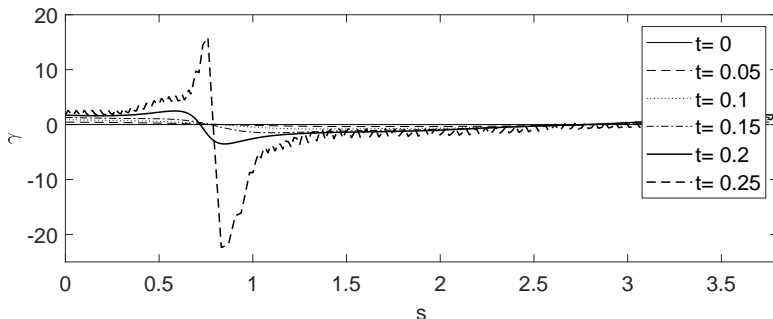The evolution of contours for cases with Atwood numbers, $A = 0.3$, 0.5, 0.7, is shown in

Figure 8: Vortex sheet strength γ evolving into a shock-like profile. $A = 0.7$, $Fr = 0.3$ and $We = \infty$.

figure 7. In each case, we observe that contours were deformed from their initially circular shape. The lower half of the contour bent inward and the ambient fluid squeezed into the vortical core from below. Similar behaviour was obtained in Lundgren & Mansour (1991) for a spherical vortex bubble. As the contour for $A = 0.3$ and 0.5 evolves, two counter-rotating roll-ups develop. These are due to the dot product of local tangent and gravity, i.e. $\mathbf{t} \cdot \hat{\mathbf{z}}$, in the buoyancy term. The dot product is negative when the local tangent of the contour points down and positive when it points up. As the result, the source term has different signs on the left and right half of the contour. Once the vortex sheet is created by the baroclinic torque, it rotates in opposite directions. In the $A = 0.3$ and 0.5 cases, a mushroom-like structure can be seen when the contour evolves for a longer time. We did not include surface tension in the calculations here, but we anticipate that surface tension will suppress the development of roll-up. The mushroom structure did not appear for the $A = 0.7$ case, when the calculation stopped earlier than the former two cases, before any roll-up will appear. Since roll-up did not happen, the failure of the calculation does not seem to be related to the curvature singularities we discussed above. We look into the vortex sheet strength profile for $A = 0.7$ by plotting γ along the contour. We found that as the vortex sheet strength evolved, a shock-like discontinuity developed in its profile, as shown in figure 8. This originates from the quadratic term in the vortex sheet equation. For large enough Atwood number, the evolution equation for γ resembles the inviscid Burgers equation, which is known to allow shocks. The whole calculation then broke down once the discontinuity appeared in γ and subsequently spread to other numerical quantities.

Calculations were carried out in a wider parameter space for A and Fr, as shown in figure 9. The dotted curves are lines of constant A/Fr^2 that represent the strength of buoyancy. The Weber number is infinite. The contours are shown at the moment when the magnitude of highest filtered mode $|k| = N/3$ is in the same order to the magnitude of mode $|k| = 1$ so that failure of the calculations is imminent. The bottom left corner is where A and Fr are both small, and hence it is the Boussinesq limit. The cases with $A = 1$ on the right have more limited calculation time, since the nonlinear term $\partial \gamma^2 / \partial \xi$ becomes important and leads to a shock-like discontinuity in γ as discussed above. On the top of the chart, the computations are also very limited. In this regime, the vortex sheet equation is dominated by the dynamic-coupled and the quadratic terms while buoyancy is weak. Our numerical scheme is not very stable in this regime. In general, contours on the bottom-left portion of the domain are more manageable for numerical calculation.

The aspect ratio of the ring S was then varied from 0.6 to 0.2, 0.1 and 0.05. As shown
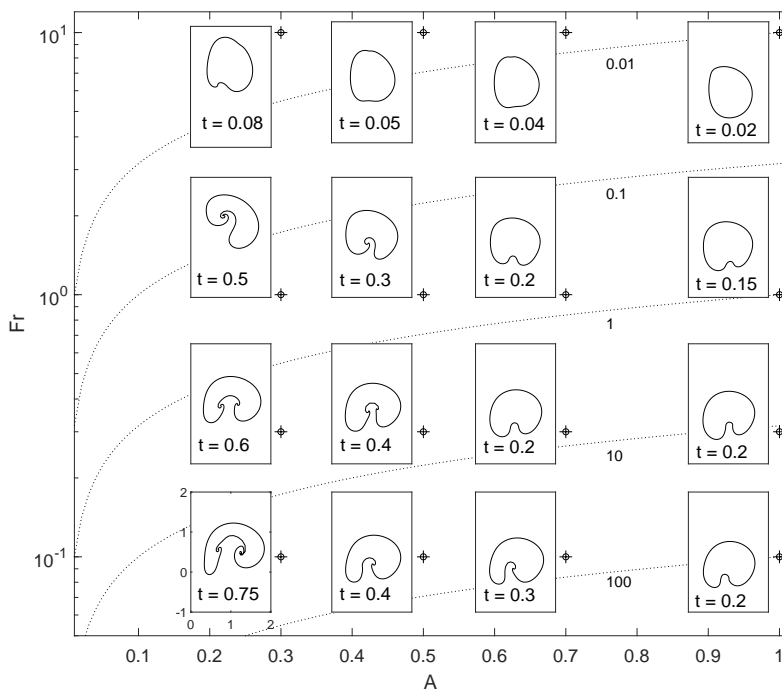
Figure 9: Contour at the time indicated in each inset for a range of (A, Fr). The dotted curves have constant A/Fr^2 values of 0.01, 0.1, 1, 10, 100; $S = 0.6$ and $We = \infty$ are kept constant.

in figure 10, the contour is still bending inward from its bottom, but its inner half (closer to the axis of symmetry) is lifted up compared to the $S = 0.6$ case. The mushroom-like structure is not observed during the calculation. Calculations stopped because a shock-like profile of γ formed. When the aspect ratio dropped to 0.05, the dynamic became different from those with larger S. The contour maintained its near-circular shape until $t = 0.4$, then it started to deform into an elliptic shape. Then it paused its upward motion and stayed near $(1.08, 0.11)$ during $t = 0.4$–0.5. From $t = 0.7$ it resumed its upward motion, and a small tip appeared on the top of the contour before the calculation failed. In figure 11, we plot the centroid (defined in § 4.4) for $S = 0.05$. Initially Z_c increases linearly and then is nearly constant around $t = 0.4$–0.5, before increasing again. Before the contour deviated from its circular shape, the initial vertical velocity can be estimated using the thin ring model from Chang & Llewellyn Smith (2018):

$$\frac{\partial Z_c}{\partial t} = \frac{\Gamma}{4\pi\mathcal{R}}\left(\ln\frac{8}{S} - \frac{1}{2} + \frac{1}{4}\frac{\rho_2}{\rho_1}\right),$$

where Γ is the circulation and the expansion rate of the ring can be estimated by

$$\frac{\partial R_c}{\partial t} = \left(1 - \frac{\rho_2}{\rho_1}\right)\frac{\pi a^2 g}{\Gamma},$$

which are plotted by dashed lines in figure 11 for $S = 0.05$. Then R_c expanded rapidly before $t = 0.4$, then diminished a little before resuming its expansion. While the current
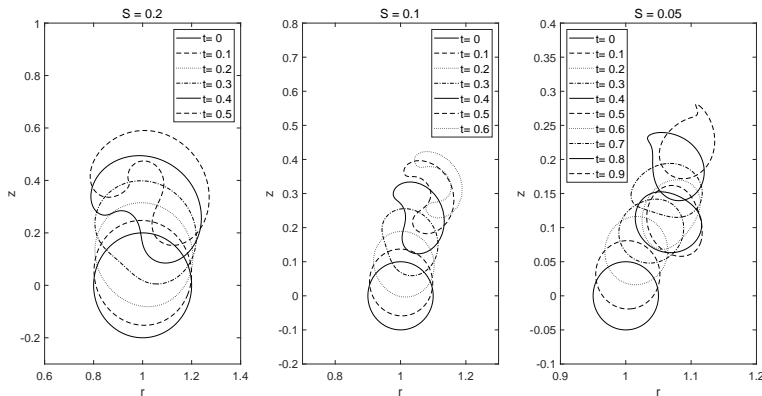
Figure 10: Evolution of contour with aspect ratio $S = 0.2$, 0.1, 0.05, respectively. Other parameters are kept constant: $A = 0.3$, $Fr = 0.3$ and $We = \infty$.
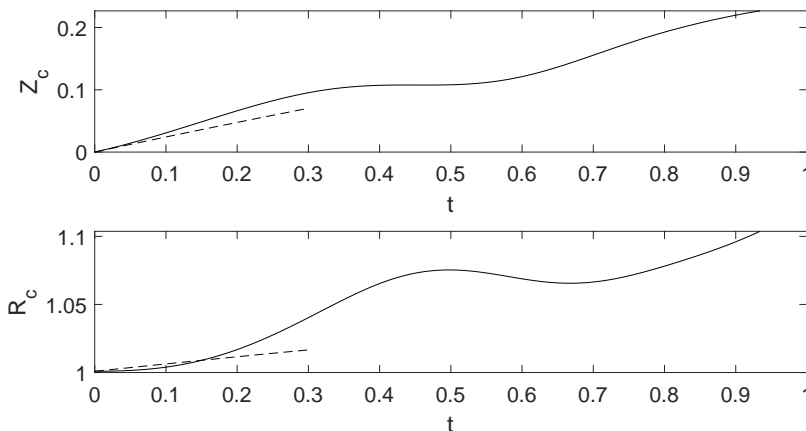

Figure 11: Evolution of the centroid for the case with aspect ratio $S = 0.05$ shown in figure 10. Dashed lines are estimations using thin ring model.

calculations eventually fail, for a thin ring Pedley (1968) has shown that the radius of a buoyant ring increases as $\sqrt{t}$ when $t \to \infty$.

The vertical acceleration can be calculated by differentiating $\partial Z_c/\partial t$:

$$
\begin{aligned}
\frac{\partial^2 Z_c}{\partial t^2} &= -\frac{\Gamma}{4\pi\mathcal{R}^2}\left(\ln\frac{8}{S} - \frac{1}{2} + \frac{1}{4}\frac{\rho_2}{\rho_1}\right)\frac{\partial\mathcal{R}}{\partial t} - \frac{\Gamma}{4\pi\mathcal{R}}\frac{1}{S}\frac{\partial S}{\partial t}, \\
&= \frac{a^2 g}{4\mathcal{R}^2}\left(1 - \frac{\rho_2}{\rho_1}\right)\left(-\ln\frac{8}{S} + 2 - \frac{1}{4}\frac{\rho_2}{\rho_1}\right),
\end{aligned}
\tag{4.1}
$$

where the continuity equation gives $-2S^{-1}\partial S/\partial t = 3\mathcal{R}^{-1}\partial\mathcal{R}/\partial t$. Scaling (4.1) by U_c^2/a_0, the acceleration of a thin ring due to buoyancy is

$$
\left(1 - \frac{\rho_2}{\rho_1}\right)\frac{S^2}{4Fr^2}\left(-\ln\frac{8}{S} + 2 - \frac{1}{4}\frac{\rho_2}{\rho_1}\right).
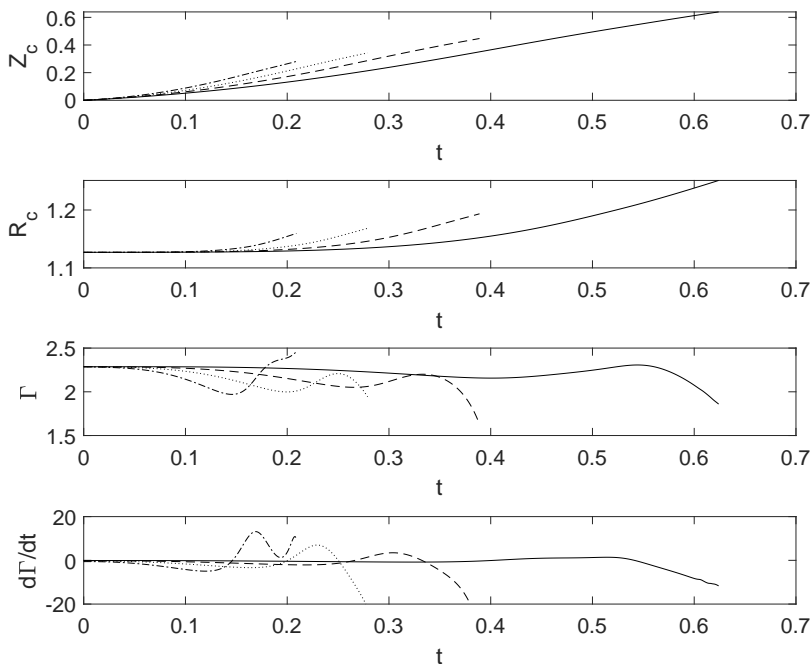$$

Figure 12: Evolution of centroid (R_c, Z_c), circulation Γ and its derivative $\mathrm{d}\Gamma/\mathrm{d}t$ for $A = 0.3$; —, $A = 0.5$; - -, $A = 0.7$; $\cdots$, $A = 1$; $\cdot$ −. The other dimensionless numbers are $S = 0.6$, $Fr = 0.3$, $We = \infty$.

4.4. *Centroid and circulation*

We now present some quantitative results of contour evolution. Two integral quantities are used to quantify vortex motion and dynamics: the centroid and the circulation. The centroid of the vortical core is calculated using the formula (Pozrikidis 1986):

$$R_c^2 = \frac{\oint R^3 Z \mathbf{t} \cdot \mathbf{r} \, \mathrm{d}s}{\oint RZ \mathbf{t} \cdot \mathbf{r} \, \mathrm{d}s}, \quad Z_c = \frac{\oint R^3 Z^2 \mathbf{t} \cdot \mathbf{r} \, \mathrm{d}s}{2 \oint R^3 Z \mathbf{t} \cdot \mathbf{r} \, \mathrm{d}s}. \tag{4.2}$$

To control the strength of buoyancy, we set $Fr = 0.3$ and increase A from 0.3 to 1. Figure 12 shows the evolution of the centroid (R_c, Z_c). Buoyancy increases the speed of the vortex ring in the vertical direction and expands the ring. The speed of translation for $A = 0.3$ is a constant and Z_c is almost linear in time. When A is increased, the ring accelerates slightly. The slope of Z_c becomes steeper in time for $A > 0.3$, which indicates that a stronger buoyancy accelerates the vortex ring in the vertical direction. The growth of R_c shown in figure 12 indicates the expansion of the vortex ring, which increases as buoyancy strengthens.

The evolution of circulation Γ and its derivative are plotted in figure 12. The circulation of a buoyant vortex ring has contributions from both patch and sheet, with

$$\Gamma = \Gamma_p + \oint \gamma \, \mathrm{d}\xi, \quad \Gamma_p = \Omega \oint R^2 \mathbf{t} \cdot \mathbf{z} \, \mathrm{d}s, \tag{4.3}$$

where Γ_p is the part from the vortex patch computed using the contour integral given in
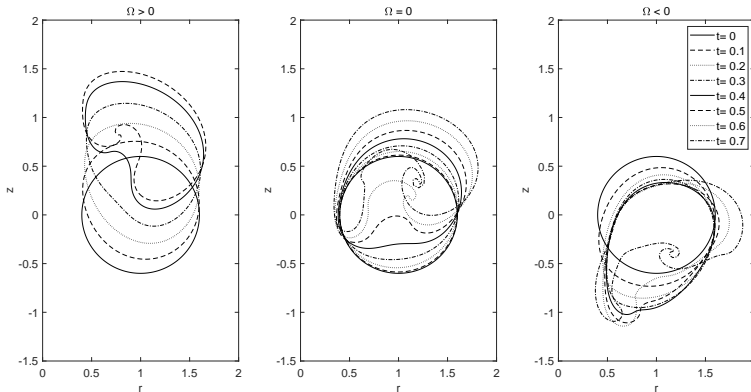
Figure 13: Evolution of contour for positive, zero, and negative Ω from left to right respectively. $S = 0.6$, $A = 0.3$, $We = \infty$.

Pozrikidis (1986). The sign is reversed because we evaluate the integral clockwise. The circulation contributed by the vortex sheet is calculated by integrating γ along the contour. When there is no density difference and buoyancy, circulation is conserved according to Kelvin's circulation theory, i.e. $\Gamma = \Gamma_p$ and $d\Gamma/dt = 0$. The material derivative of Γ can be obtained by integrating (2.32) along the contour. For the Boussinesq case, there is only one term on the right-hand side,

$$\frac{d\Gamma}{dt} = -2\frac{A}{Fr^2} \oint L\mathbf{t} \cdot \mathbf{z}\, d\xi, \tag{4.4}$$

and $d\Gamma/dt$ is a function of the shape of the contour only. The shape is characterized by the local tangent $\mathbf{t}$ and the metric L. For the non-Boussinesq case, $d\Gamma/dt$ also requires integration over the dynamic-coupled and the quadratic terms, which are functions of γ and the dynamics of the contour. For $A = 0.3$, the rate of change of the circulation is approximately zero in figure 12. For larger values of A, the circulation decreases. This can be compared to the contours shown in figure 9. As the contours evolve and are deformed into two lobes, the vorticity on the contour is swept into the region between the two lobes and accumulate. The net effect is a negative circulation contributed by the vortex sheet. With Γ_p kept constant, the total circulation then drops. The circulation for $A = 1$ and $Fr = 0.3$ reached a minimum at $t = 0.145$ then increases beyond its initial value.

4.5. *Calculations for $\Omega \leqslant 0$*

The results we have shown so far are for $\Omega > 0$, for which the ring is moving upward against gravity. Other possibilities include $\Omega = 0$, when the vorticity inside the core vanishes and the vortex ring is "hollow", and $\Omega < 0$, for which the vortex ring moves downward when there is no buoyancy. We calculate both cases and compare them to the $\Omega > 0$ case in figure 13. For $\Omega > 0$ and $\Omega < 0$, we set $|\Omega| = 6.7392$ so that $Fr = 1$. The Froude number is greater than that used in figure 7, so the bulk vorticity inside the core is more dominant here than the cases shown in figure 7 ($Fr = 0.3$). The contour still bent inward from the bottom, but it did not evolve into two counter-rotating rollups like a mushroom structure. Instead a single rollup, located on the inner half (closer to the axis of symmetry) and rotating counter-clockwise, appeared first. The outer half (away from the axis of symmetry) moved slower and is dragged behind the inner half. When the continuous vorticity Ω inside vanishes, we observe a different behaviour: a rollup
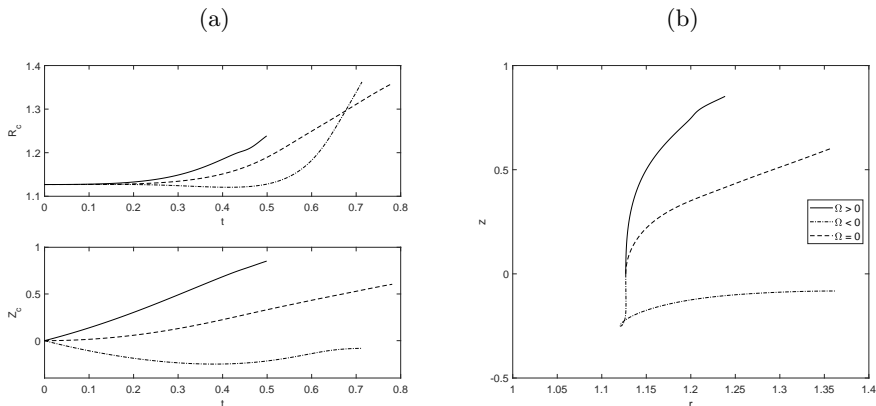
(a)   (b)

Figure 14: Evolution of (a) centroid: (R_c, Z_c) and (b) the trajectories for $\Omega > 0$; —, $\Omega = 0$; - -, $\Omega < 0$; · −.

rotating clockwise appeared on the outer half of the contour earlier than its counter-clockwise counterpart. This might show that the two counter-rotating rollups appeared in the $Fr = 0.3$ are associated with the dominant balance between the bulk vorticity (vortex ring) and the vortex sheet (density and gravity) respectively. When the bulk vorticity dominates, the counter-clockwise rollup appears, while when vortex sheet dominates the clockwise rollup emerges first. The expansion of the ring radius and the vertical speed of the ring are also decreased when the continuous vorticity vanishes (figure 14).

If we reverse the direction in which vortex ring travels by setting $\Omega = -6.7392$, the contour moved downward initially as shown in figure 13. This downward movement reversed at $t \approx 0.4$ where Z_c started to increase (figure 13). A clockwise rollup emerged and the end of calculation at $t = 0.7$ indicating vortex sheet grown to a stage that took over the dominance on the evolution of the contour. A long lobe close to the axis of symmetry can be seen being dragged behind as the bulk motion of the contour moves up.

4.6. *Energy conservation*

The kinetic energy of the flow associated with the vortex sheet is

$$T_s = (\rho_1 - \rho_2)\,\pi \oint \psi\,\mathbf{u}\cdot\mathbf{t}L\,\mathrm{d}\xi + (\rho_1 + \rho_2)\,\pi \oint \frac{\psi\gamma}{2}\,\mathrm{d}\xi, \qquad (4.5)$$

while the contribution from vortex patch can be calculated as a contour integral, as in (A3) of Pozrikidis (1986). The potential energy is

$$U = \pi(\rho_2 - \rho_1)g \oint RZ^2 \frac{\partial R}{\partial \xi}\,\mathrm{d}\xi. \qquad (4.6)$$

(See appendix B for detailed derivations.) In the absence of surface tension, the total energy (kinetic plus potential) is conserved under inviscid dynamics. The volume, which should also be constant in time, is numerically well conserved. For $\rho_1 = \rho_2$ and for the Boussinesq case shown in figure 15(a,c) respectively, this is true for energy. In the non-Boussinesq case, the numerical conservation of total energy is limited (see figure 15 b). It is conserved well until a certain time of integration, which decreases as A increases. For $A = 0.3$ shown in figure 15(b), total energy is conserved until around $t = 0.35$, whereas it is conserved when $t < 0.6$ for $A = 0.1$ and when $t < 0.12$ for $A = 0.7$. The numerical
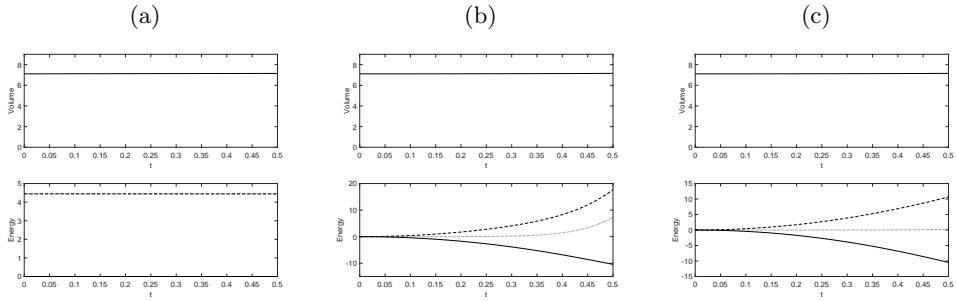
Figure 15: $\Omega = 0$, (a) $A = 0$; (b) $A = 0.3$; (c) Boussinesq calculation for $A = 0.3$. Potential energy; —, kinetic energy; - -, potential plus kinetic energy; $\cdots$.

failure of energy conservation must be due to the extra terms in the non-Boussinesq cases: the dynamic-coupled term ($\mathbf{t} \cdot d\mathbf{u}/dt$) and the quadratic term ($\partial \gamma^2 / \partial \xi$). The numerical problem could be due to a number of reasons including the desingularisation used in the numerical method, the growth of γ and the possible appearance of singularities discussed in §4.2 (see figure 6). We also observed the Fourier spectrum filling up in figure 5: the numerical growth of high modes is correlated to the failure of energy conservation. Further study of the limitations of energy convervation is left as future work.

5. Conclusions

We have presented theoretical and numerical results on the motion of a buoyant vortex ring in the non-Boussinesq regime. We derived a vortex sheet equation in (2.26) from the Euler equation. A set of coupled integro-differential equations, (2.3), (2.9), (2.11) and (2.26), is used to calculate the motion of a buoyant vortex ring. The nondimensionalized vortex sheet equation in (2.32) contains three dimensionless parameters: the Atwood number, A, the Froude number, Fr and the Weber number, We, representing different physical effects. When A and Fr are both small, the flow is in the Boussinesq limit; the vortex sheet is dominated by the gravity term and decoupled from the dynamics of the contour. The problem moves into the non-Boussinesq regime when A and Fr becomes moderate to large. In this regime, the γ equation is coupled with $d\mathbf{u}/dt$. The apparent emergence of curvature singularities limits the validity in time of our numerical calculations, as discussed in §4.2

Our numerical results show that the contour can deform drastically when the vortex sheet is present. Numerical results are obtained for both the Boussinesq and non-Boussinesq cases where the Atwood and the Froude numbers are small to moderate. Calculations for large Froude number and Atwood number close to one have been attempted but the results are very limited. In §4.3 we pointed out that a shock-like discontinuity in the vortex sheet strength γ leads to numerical failure for those cases. This does not appear to be a curvature singularity, although this may be an artifact of the blob method, since Baker & Xie (2011) showed curvature singularities approaching the real axis in the complex plane for $A = 1$. Our results for small to moderate Atwood and Froude numbers show how the motion of vortex rings deviate from a classic steady solution into nonlinear evolution when adding density effect and buoyancy. The core of the vortex ring is deformed in such a fashion that the surrounding fluid squeezes in from the bottom. In some cases, a mushroom-like pattern develops with two counter-rotating roll-ups on the contour. Surface tension is given in our formulation, but we did not include it in

the numerical results. The numerics for surface tension requires careful treatment, so the present work emphasized the effects of density and buoyancy. Our results give insights into flows dominated by buoyancy and vorticity, which have implications on geophysical and environmental fluid dynamics. Possible future work includes investigations of the stability of these vortex rings, the effect of surface tension, and as an investigation of curvature singularities in axisymmetry. These last two work would require the development of a numerical method that is robust in the presence of surface tension and that does not use blobs, e.g. adapting the midpoint rule used by Baker & Nachbin (1998) to work in axisymmetric geometry.

Declaration of Interests. The authors report no conflict of interests.

Appendix A. Calculation of $\mathbf{t} \cdot \mathrm{d}\mathbf{u}/\mathrm{d}t$

Taking the material derivative $\mathrm{d}/\mathrm{d}t$ of (2.9) yields

$$\frac{\mathrm{d}u_{p,r}}{\mathrm{d}t} = -\frac{\Omega}{R^2}u_r \oint R'\cos\theta' G \mathrm{d}s' + \frac{\Omega}{R} \oint \left(u_r'\cos\theta' G - R'\sin\theta'\frac{\mathrm{d}\theta'}{\mathrm{d}t}G + R'\cos\theta'\frac{\mathrm{d}G}{\mathrm{d}t} \right)\mathrm{d}s', \tag{A 1}$$

$$\frac{\mathrm{d}u_{p,z}}{\mathrm{d}t} = \Omega \oint \left[(u_z' - u_z)\cos\theta' H - (Z' - Z)\sin\theta'\frac{\mathrm{d}\theta'}{\mathrm{d}t}H + (Z' - Z)\cos\theta'\frac{\mathrm{d}H}{\mathrm{d}t} \right]\mathrm{d}s' \\ - \Omega \oint \left(\cos\theta'\frac{\mathrm{d}\theta'}{\mathrm{d}t}G + \sin\theta'\frac{\mathrm{d}G}{\mathrm{d}t} \right)\mathrm{d}s'. \tag{A 2}$$

The primes indicate dummy variables in the integrals and (R, Z) is the location of Lagrangian point. The first subscript represent the contribution from the vortex patch or vortex sheet, while the second subscript indicates the velocity components. We do the same for (2.11) for the sheet:

$$\frac{\mathrm{d}u_{s,r}}{\mathrm{d}t} = -\frac{1}{R} \oint \frac{\mathrm{d}\gamma}{\mathrm{d}t}\frac{\partial G}{\partial Z}\mathrm{d}\xi' + \frac{1}{R^2}u_r \oint \gamma\frac{\partial G}{\partial Z}\mathrm{d}\xi' - \frac{1}{R} \oint \gamma\frac{\mathrm{d}}{\mathrm{d}t}\left(\frac{\partial G}{\partial Z} \right)\mathrm{d}\xi', \tag{A 3}$$

$$\frac{\mathrm{d}u_{s,z}}{\mathrm{d}t} = \frac{1}{R} \oint \frac{\mathrm{d}\gamma}{\mathrm{d}t}\frac{\partial G}{\partial R}\mathrm{d}\xi' - \frac{1}{R^2}u_r \oint \gamma\frac{\partial G}{\partial R}\mathrm{d}\xi' + \frac{1}{R} \oint \gamma\frac{\mathrm{d}}{\mathrm{d}t}\left(\frac{\partial G}{\partial R} \right)\mathrm{d}\xi'. \tag{A 4}$$

Taking the dot product of $d\mathbf{u}/dt$ with the tangent $\mathbf{t} = L^{-1}(\partial R/\partial\xi, \partial Z/\partial\xi)$ yields (2.27) with

$$
\begin{aligned}
f(R, Z, \gamma, \mathbf{u}) = &\frac{1}{L}\frac{\partial R}{\partial\xi}\left[\frac{\Omega}{R}\oint\left(u_r'\cos\theta' G - R'\sin\theta'\frac{d\theta'}{dt}G + R'\cos\theta'\frac{dG}{dt}\right)ds'\right. \\
&\left. -\frac{\Omega}{R^2}u_r\oint R'\cos\theta' G ds' - \frac{1}{R^2}u_r\oint\gamma\frac{\partial G}{\partial Z}d\xi' - \frac{1}{R}\oint\gamma\frac{d}{dt}\left(\frac{\partial G}{\partial Z}\right)d\xi'\right] \\
&+\frac{1}{L}\frac{\partial Z}{\partial\xi}\left\{-\Omega\oint\left(\cos\theta'\frac{d\theta'}{dt}G + \sin\theta'\frac{dG}{dt}\right)ds'\right. \\
&+\Omega\oint\left[(u_z' - u_z)\cos\theta' H - (Z' - Z)\sin\theta'\frac{d\theta'}{dt}H + (Z' - Z)\cos\theta'\frac{dH}{dt}\right]ds' \\
&\left.+\frac{1}{R^2}u_r\oint\gamma\frac{\partial G}{\partial R}d\xi' + \frac{1}{R}\oint\gamma\frac{d}{dt}\left(\frac{\partial G}{\partial R}\right)d\xi'\right\}.
\end{aligned}
\tag{A 5}
$$

Appendix B. Expressions for the kinetic and potential energies

Using (3.11.4) in Saffman (1992), the kinetic energy in a volume V is given by

$$
T = \frac{1}{2}\rho\int_V|\mathbf{u}|^2\,dV = \frac{1}{2}\rho\left[\int_V\mathbf{A}\cdot\boldsymbol{\omega}\,dV - \int_S(\mathbf{u}\times\mathbf{A})\cdot\mathbf{n}\,dS\right],
\tag{B 1}
$$

where the unit normal vector $\mathbf{n}$ points out from the volume V enclosed by the surface S, and the vector potential gives $\mathbf{u} = \nabla\times\mathbf{A}$. For axisymmetric flows in (r, ϕ, z),

$$
\boldsymbol{\omega} = \omega_\phi\hat{\boldsymbol{\phi}}, \quad \mathbf{A} = \frac{\psi}{r}\hat{\boldsymbol{\phi}}
$$

and

$$
dV = r\,dr\,d\phi\,dz, \quad dS = r\,d\phi\,ds,
$$

where the surface S is a torus and s is the arc length of a contour on the rz plane. Integrating over ϕ gives

$$
T = \pi\rho\left[\iint\omega_\phi\psi\,dr\,dz - \oint(\mathbf{u}\times\mathbf{A})\cdot\mathbf{n}r\,ds\right].
\tag{B 2}
$$

For the setting shown in figure 1, the kinetic energies outside and inside the vortex are

$$
T_1 = -\pi\rho_1\oint(\mathbf{u}_1\times\mathbf{A})\cdot(-\mathbf{n})r\,ds,
\tag{B 3}
$$

and

$$
T_2 = \pi\rho_2\left[\iint\omega_\phi\psi\,dr\,dz - \oint(\mathbf{u}_2\times\mathbf{A})\cdot\mathbf{n}\,r\,ds\right],
\tag{B 4}
$$

respectively. The total kinetic energy is $T = T_1 + T_2$. The double integral in T_2 corresponds to the vortex patch,

$$
T_p = \pi\rho_2\iint\omega_\phi\psi\,dr\,dz = \pi\rho_2\Omega\iint\psi r\,dr\,dz,
\tag{B 5}
$$

and can be calculated using (A3) in Pozrikidis (1986) as a contour integral. The remaining integrals in T are related to the vortex sheet:

$$
T_s = \pi\rho_1\oint(\mathbf{u}_1\times\mathbf{A})\cdot\mathbf{n}\,r\,ds - \pi\rho_2\oint(\mathbf{u}_2\times\mathbf{A})\cdot\mathbf{n}r\,ds.
\tag{B 6}
$$

By using $\mathbf{u}_i = u_i \hat{\mathbf{r}} + v_i \hat{\mathbf{z}}$ and $\mathrm{d}s = L\,\mathrm{d}\xi$, we obtain

$$(\mathbf{u}_i \times \mathbf{A}) \cdot \mathbf{n} = \frac{\psi}{r} \left(u_i \frac{\partial R}{\partial \xi} + v_i \frac{\partial Z}{\partial \xi} \right) \frac{1}{L} = \frac{\psi}{r} \mathbf{u}_i \cdot \mathbf{t}. \tag{B7}$$

Then (B6) becomes

$$T_s = \pi \rho_1 \oint \psi \mathbf{u}_1 \cdot \mathbf{t}\mathrm{d}s - \pi \rho_2 \oint \psi \mathbf{u}_2 \cdot \mathbf{t}\mathrm{d}s, \tag{B8}$$

$$= (\rho_1 - \rho_2)\pi \oint \psi \mathbf{u} \cdot \mathbf{t}\ L\mathrm{d}\xi + (\rho_1 + \rho_2)\frac{\pi}{2} \oint \psi \gamma \mathrm{d}\xi. \tag{B9}$$

If $\rho_1 = \rho_2 = \rho$,

$$T_s = \pi \rho \oint \psi(\mathbf{u}_1 - \mathbf{u}_2) \cdot \mathbf{t}L\mathrm{d}\xi, = \pi \rho \oint \psi \gamma\,\mathrm{d}\xi, \tag{B10}$$

where $\gamma = L(\mathbf{u}_1 - \mathbf{u}_2) \cdot \mathbf{t}$. Taking $\rho = 1$, this is identical to (2.36) in Hattori & Moffatt (2006). Finally, the potential energy is calculated from

$$U = 2\pi(\rho_2 - \rho_1)g \iint rz\mathrm{d}r\mathrm{d}z = \pi(\rho_2 - \rho_1)g \oint RZ^2 \frac{\partial R}{\partial \xi}\mathrm{d}\xi. \tag{B11}$$

REFERENCES

BAKER, G.R., CAFLISCH, R. & SIEGEL, M. 1993 Singularity formation during Rayleigh–Taylor instability. *J. Fluid Mech.* **252**, 51–78.

BAKER, G.R., MEIRON, D.I. & ORSZAG, S.A. 1982 Generalized vortex methods for free-surface flow problems. *J. Fluid Mech.* **123**, 477–501.

BAKER, G.R. & MOORE, D.W. 1989 The rise and distortion of a two-dimensional gas bubble in an inviscid liquid. *Phys. Fluids* A **1**, 1451–1459.

BAKER, G.R. & NACHBIN, A. 1998 Stable methods for vortex sheet motion in the presence of surface tension. *SIAM J. Sci. Comput.* **19**, 1737–1766.

BAKER, G.R. & XIE, C. 2011 Singularities in the complex physical plane for deep water waves. *J. Fluid Mech.* **685**, 83–116.

BLYTH, M., RODRIGUEZ-RODRIGUEZ, J. & SALMAN, H. 2014 Buoyant Norbury's vortex rings. In *Bulletin of the American Physical Society*, *Div. Fluid Dyn.*, vol. 59.

CHANG, C. & LLEWELLYN SMITH, S. G. 2018 The motion of a buoyant vortex filament. *J. Fluid Mech.* **857**, R1.

CHEN, L., GARIMELLA, S.V., REIZES, J.A. & LEONARDI, E. 1999 The development of a bubble rising in a viscous liquid. *J. Fluid Mech.* **387**, 61–96.

CHENG, M., LOU, J. & LIM, T.T. 2013 Motion of a bubble ring in a viscous fluid. *Phys. Fluids* **25**, 067104.

COWLEY, S.J., BAKER, G.R. & TANVEER, S. 1999 On the formation of Moore curvature singularities in vortex sheets. *J. Fluid Mech.* **378**, 233–267.

DRITSCHEL, D.G. 1989 Contour dynamics and contour surgery: Numerical algorithms for extended, high-resolution modelling of vortex dynamics in two-dimensional, inviscid, incompressible flows. *Comput. Phys. Rep.* **10**, 77–146.

FRAENKEL, L.E. 1972 Examples of steady vortex rings of small cross-section in an ideal fluid. *J. Fluid Mech.* **51**, 119–135.

HATTORI, Y. & MOFFATT, H. K. 2006 Evolution of toroidal magnetic eddies in an ideal fluid. *J. Fluid Mech.* **558**, 253–279.

HICKS, W. M. 1884 On the steady motion and small vibrations of a hollow vortex. *Phil. Trans. R. Soc. Lond.* A **175**, 161–195.

HOU, T.Y., LOWENGRUB, J.S. & SHELLEY, M.J. 1994 Removing the stiffness from interfacial flows with surface tension. *J. Comput. Phys.* **114**, 312–338.

ISERLES, A. 2009 *A First Course in the Numerical Analysis of Differential Equations*. Cambridge University Press.

Kelvin, Lord 1867 The translatory velocity of a circular vortex ring. *Phil. Mag.* **33**, 511–512.

Krasny, R. 1986*a* Desingularization of periodic vortex sheet roll-up. *J. Comput. Phys.* **65**, 292–313.

Krasny, R. 1986*b* A study of singularity formation in a vortex sheet by the point-vortex approximation. *J. Fluid Mech.* **167**, 65–93.

Llewellyn Smith, S. G., Chang, C., Chu, T., Blyth, M., Hattori, Y. & Salman, H. 2018 Generalized contour dynamics: A review. *Reg. Chaotic Dyn.* **23**, 507–518.

Llewellyn Smith, S. G. & Hattori, Y. 2012 Axisymmetric magnetic vortices with swirl. *Commun. Nonlinear Sci. Numer. Simulat.* **17**, 2101–2107.

Lundgren, T. S. & Mansour, N. N. 1991 Vortex ring bubbles. *J. Fluid Mech.* **224**, 177–196.

Marten, K., Shariff, K., Psarakos, S. & White, D.J. 1996 Ring bubbles of dolphins. *Sci. Am.* **275**, 82–87.

Meiron, D.I., Baker, G.R. & Orszag, S.A. 1982 Analytic structure of vortex sheet dynamics. Part 1. Kelvin–Helmholtz instability. *J. Fluid Mech.* **114**, 283–298.

Moore, D.W. 1979 The spontaneous appearance of a singularity in the shape of an evolving vortex sheet. *Proc. R. Soc. Lond.* A **365**, 105–119.

Nitsche, M. 2001 Singularity formation in a cylindrical and a spherical vortex sheet. *J. Comout. Phys.* **173**, 208–230.

Nitsche, M. & Krasny, R. 1994 A numerical study of vortex ring formation at the edge of a circular tube. *J. Fluid Mech.* **276**, 139–161.

Norbury, J. 1972 A steady vortex ring close to Hill's spherical vortex. *Proc. Camb. Phil. Soc.* **72**, 253–284.

Norbury, J. 1973 A family of steady vortex rings. *J. Fluid Mech.* **57**, 417–431.

Pedley, T.J. 1968 The toroidal bubble. *J. Fluid Mech.* **32**, 97–112.

Pozrikidis, C. 1986 The nonlinear instability of Hill's vortex. *J. Fluid Mech.* **168**, 337–367.

Pullin, D.I. 1992 Contour dynamics methods. *Annu. Rev. Fluid Mech.* **24**, 89–115.

Riley, N. 1998 The fascination of vortex rings. *Appl. Sci. Res.* **59**, 169–189.

Saffman, P. G. 1992 *Vortex Dynamics*. Cambridge University Press.

Shariff, K. & Leonard, A. 1992 Vortex rings. *Annu. Rev. Fluid Mech.* **24**, 235–279.

Shariff, K., Leonard, A. & Ferziger, J. 1989 Dynamics of a class of vortex rings. *Tech. Rep.* 102257. NASA Tech. Rep.

Shariff, K., Leonard, A. & Ferziger, J. 2008 A contour dynamics algorithm for axisymmetric flow. *J. Comput. Phys.* **227**, 9044–9062.

Shin, S., Sohn, S.-I. & Hwang, W. 2014 Simple and efficient numerical methods for vortex sheet motion with surface tension. *Int. J. Numer. Meth. Fl.* **74**, 422–438.

Shin, S., Sohn, S.-I. & Hwang, W. 2018 Vortex simulations of the Kelvin–Helmholtz instability with surface tension in density-stratified flows. *Eur. J. Mech.* B *Fluids* **67**, 168–177.

Sohn, S.-I. 2015 Stability and capillary dynamics of circular vortex sheets. *Theor. Comput. Fluid Dyn.* **29**, 291–310.

Sohn, S.-I. & Hwang, W. 2005 Numerical simulations of vortex sheet evolution in stratified shear flow. *J. Phys. Soc. Jpn.* **74**, 1472–1478.

Stock, M.J., Dahm, W.J.A. & Tryggvason, G. 2008 Impact of a vortex ring on a density interface using a regularized inviscid vortex sheet method. *J. Comput. Phys.* **227**, 9021–9043.

Trefethen, L. N. & Weideman, J. A. C. 2014 The exponentially convergent trapezoidal rule. *SIAM Review* **56**, 385–458.

Tryggvason, G. 1988 Numerical simulations of the Rayleigh–Taylor instability. *J. Comput. Phys.* **75**, 253–282.

Turner, J.S. 1957 Buoyant vortex rings. *Proc. R. Soc. Lond.* A **239**, 61–75.

Vasel-Be-Hagh, A.R., Carriveau, R. & Ting, D.S.-K. 2015*a* A ballon bursting underwater. *J. Fluid Mech.* **769**, 522–540.

Vasel-Be-Hagh, A.R., Carriveau, R., Ting, D.S.-K. & Turner, J.S. 2015*b* Drag of buoyant vortex rings. *Phys. Rev.* A **92**, 043024.

Velasco Fuentes, O. 2014 Early observations and experiments on ring vortices. *Eur. J. Mech.* B *Fluids* **43**, 166–171.

ZABUSKY, N.J., HUGHES, M.H. & ROBERTS, K.V. 1979 Contour dynamics for the Euler equations in two dimensions. *J. Comput. Phys.* **30**, 96–106.